Korean J. Chem. Eng., 40(6), 1360-1372 (2023)
DOI: 10.1007/s11814-022-1354-2

pISSN: 0256-1115
eISSN: 1975-7220

Photocatalytic degradation of the organophosphorus insecticide chlorpyrifos in aqueous suspensions using a novel activated carbon ZrO_2-ZnO nanocomposite under UV light

Soremo L Ezung, Mridushmita Baruah, Suraj Kumar, Shisak Sharma, and Dipak Sinha†

Department of Chemistry, Nagaland University, Lumami-798627, Nagaland, India
(*Received 4 July 2022 • Revised 15 November 2022 • Accepted 21 November 2022*)

Abstract−This paper describes the photocatalytic degradation of the organophosphorus insecticide chlorpyrifos in aqueous suspensions using *Schima wallichii* activated carbon/ZrO_2-ZnO (SWAC/ZrO_2-ZnO) nanocomposite in UV light. Analytical techniques such as XRD, FT-IR, TEM-SEAD, XPS, PL, and BET analyzer were used to characterize the SWAC/ZrO_2-ZnO nanocomposite. The BET surface area of the photocatalyst was found to be 223.387 m^2g^{-1}, having a total pore volume of 0.1845 cm^3g^{-1}. The photocatalytic degradation of chlorpyrifos followed pseudo-first-order rate kinetics with a half-life period ($t_{1/2}$) of 7.088 mins and K_{ap} (apparent rate constant) of 0.09778 min^{-1}. The mechanism of composite formation was explained using DFT investigations, which demonstrated a favorable immobilization of ZrO_2-ZnO on SWAC. Chemical descriptors gained from DFT investigations, such as HOMO-LUMO energy, ionization energy, dipole moment, chemical softness, and chemical hardness, supported an understanding of the relative efficiency and reactivity of ZrO_2-ZnO and SWAC/ZrO_2-ZnO towards chlorpyrifos degradation.

Keywords: SWAC/ZrO_2-ZnO Nanocomposite, Photocatalytic Degradation, UV Light Irradiation, Kinetics

INTRODUCTION

Pesticides are designed to control pests; however, their widespread use in industrial and agricultural activities has become a matter of concern as the discharges from these sources contaminate water systems. Chlorpyrifos (CPs) is a common organophosphate insecticide used in agriculture to boost production and protect crops from insects and pests. The presence of chlorpyrifos in water can cause skin irritation, headaches, nausea, respiratory failure, stomach cramps, and even death in humans [1,2]. Therefore, developing a new and efficient method of wastewater treatment is necessary to remove organic pollutants from the aqueous medium. Several novel approaches for chlorpyrifos-containing wastewater treatment have been suggested to date. These involve the application of electrochemical degradation [3], ionizing radiation [4], biodegradation [5] batch adsorption [6], and photocatalytic degradation [7]. Out of various approaches, the development of the photocatalytic technique is one of the most potential processes for the degradation of organic contaminants due to its ease of use, high efficiency, lack of secondary pollution, and low cost [8]. This method takes place in the presence of light wherein the semiconductor materials absorb the energy of a photon $\geq E_g$ (bandgap) and promotes an electron from the valence band to the conduction band. This allows for the creation of an electron in the conduction band and a positive hole in the valence band. Thus, the electron behaves as a reductant and the positive hole as an oxidant in the photocatalytic method [9].

Some of the metal oxide nanoparticle photocatalysts employed for the degradation or removal of organic compounds in aqueous media are ZnS (Zinc sulfide), TiO_2 (Titanium dioxide), ZnO (Zinc oxide), WO_3 (Tungsten trioxide), CuO (Copper oxide), and ZrO_2 (Zirconium dioxide) [10,11]. Under UV radiation, these metal oxides degrade organic compounds, transforming them into harmless end products through various steps. Out of these, ZnO has been extensively studied because of its superior photocatalytic activity, stability, non-toxicity, and low cost [12]. However, ZnO has disadvantages such as photocorrosion and instability when exposed to light. Furthermore, a high recombination rate of photogenerated holes and electrons renders the photocatalytic process ineffective [13]. As a result, ongoing attempts are being made to increase the photocatalytic activity of ZnO by coupling or doping with metal/metal oxides. The well-known metal oxide zirconium dioxide (ZrO_2) has high thermal stability, excellent corrosion resistance, a high dielectric constant, and a wide band gap energy of ~5.0 eV [14]. Although the ZrO_2 band gap value is insufficient for degradation studies, its monoclinic phase and composite form help to improve the photocatalytic activity. Further presence of ZrO_2 in ZnO/ZrO_2 complexes increases the generation of *OH radicals, which is also responsible for the increase in photoactivity. Therefore, the presence of ZrO_2 can strengthen the thermo-mechanical and chemical stability of ZnO. Simultaneously, the presence of ZnO can reduce the band gap of ZrO_2 [15]. In addition, ZnO undergoes dissolution at lower pH, but when coupled with ZrO_2 it can improve the dissolution resistance at lower pH as reported [16].

Numerous researchers have concluded that incorporating an adsorbent and a photocatalyst system improves the removal percentage of organic pollutants [17-19]. Activated carbon (AC) is a type of co-adsorbent widely utilized as key support for the photocatalyst in the treatment of wastewater through photocatalytic deg-

†To whom correspondence should be addressed.
E-mail: dipaksinha@gmail.com

radation [20]. AC having high adsorption capacity is more preferable as an adsorbent support system for photocatalyst as it can easily absorb organic pollutant molecules close to the photocatalytic sites during the adsorption-degradation process [21]. Metal oxide nanoparticles with AC show excellent adsorbence, which provides a large number of active sites that can interact chemically with the adsorbents, thereby enhancing chemisorption [22]. However, earlier reported combinations were based on single photocatalyst systems rather than multiple heterojunctions, which might significantly enhance photocatalytic performance through electron-hole separation and better light absorption. Thus, in the present work, we report a novel nanocomposite that integrates AC with ZrO_2- ZnO photocatalyst.

Quantum chemical approaches have now shown to be a viable means of understanding the quantitative structure-activity connection and providing a theoretical foundation for the fast selection of highly competent materials [23]. Density functional theory (DFT) is one such quantum mechanical modeling approach used to study the electronic structure, properties, reactivity, and stability of atoms and molecules [24]. Employing these approaches, several researchers have succeeded in anticipating the theoretical reasoning of the reactivity and interaction features of nanomaterials [25]. Therefore, the current work strives to provide a theoretical basis to explain the reactivity of the AC nanocomposite toward CPs degradation.

The goal of this research was to investigate the photodegradation of CPs in aqueous solutions utilizing ZrO_2-ZnO nanoparticles as a catalyst supported on *Schima wallichii* activated carbon. Theoretical investigations were utilized to support experimental data and to study the reactivity towards CPs degradation using water as the solvent medium.

EXPERIMENTAL SECTION

Zinc acetate (Zn $(CH_3COO)_2{\cdot}H_2O$), Zirconium dioxide (ZrO_2) (The properties of the ZrO_2 compound are given in supplementary Table S1), and other chemicals such as HCl, NaOH, and KOH were utilized in the present study and were purchased from Sigma-Aldrich. Co., India. Tricel (20% chlorpyriphos) was purchased from Sumitomo Chemical India Ltd. The raw material *Schima wallichii* fruit utilized for this experiment was obtained directly from Nagaland University, Lumami Campus (26°28′29″ N, 94°50′58″ E).

1. Synthesis of Activated Carbon

Activated carbon was synthesized using *Schima wallichii* biomass and KOH as an activating agent. *Schima wallichii* activated carbon is referred to as SWAC in all further discussions in this paper. In a typical preparation, the collected *Schima wallichii* biomass was properly cleaned with double-distilled water and oven-dried. Dried samples were carbonized by employing a muffle furnace at 600 °C for 1 hour under static conditions in a self-generated atmosphere followed by grinding the carbonized sample into a powder form and sieved before KOH activation. For activation, an aqueous solution of KOH was prepared by dissolving 20 g of KOH in double-distilled water. The impregnation was carried out by mixing KOH solution and 10 g carbonized sample in a ratio of 2 : 1 [26]. The mixture was then stirred for about 1 hour and oven-dried at 105 °C for 24. The mixture was further pyrolyzed in a muffle furnace at 700 °C for 1 hour under static conditions in a self-generated atmosphere for the activation process. Afterward, the sample was then washed with 0.1 M NaOH and 0.1 M HCl followed by doubled-distilled water until the residual solution attained a neutral pH. The prepared sample was dried in an oven and stored in containers for further analysis.

2. Preparation of ZrO_2-ZnO Nanocomposite

To prepare a ZrO_2-ZnO nanocomposite, 2.2 g of Zn $(CH_3COO)_2{\cdot}H_2O$ and 0.5 g of ZrO_2 were added to 100 mL double-distilled water while vigorously stirred for 30 mins at room temperature. The pH of the mixture was adjusted by adding 2 M NH_4OH solution until the pH reached 9. The mixture solution was then sonicated for 30 mins to attain a homogeneous mixture [27]. The mixture was then subjected to a stainless Teflon-lined autoclave for the hydrothermal process in an oven at the temperature of 160 °C for ~12 hours. The product was centrifuged, filtered, and washed multiple times with double-distilled water. Finally, after drying in an oven at 60 °C overnight ZrO_2-ZnO nanocomposite was obtained.

3. Synthesis of SWAC/ZrO_2-ZnO Nanocomposite

For the synthesis of SWAC/ZrO_2-ZnO nanocomposite, the mixture of 0.5 g of ZrO_2-ZnO nanocomposite and 1 g of the prepared SWAC were dispersed in 100 ml double-distilled water, and the mixture was agitated for 30 mins at room temperature. Afterward, the precursor mixture was sonicated for about 30 mins to attain a homogeneous mixture. The SWAC/ZrO_2-ZnO nanocomposite was further subjected to a Teflon-lined autoclave for ~12 hours at 160 °C in an oven. Once the hydrothermal process was done, the solution was centrifuged washed with double-distilled water several times, and dried in an oven at 65 °C for 24 hours. The synthesized SWAC/ZrO_2-ZnO nanocomposite was further characterized and its application for the degradation of chlorpyriphos was investigated.

4. Characterization of the SWAC/ZrO_2-ZnO

Characterization of SWAC/ZrO_2-ZnO nanocomposite involved using different analytical techniques. The structure of the SWAC/ZrO_2-ZnO nanocomposite was assessed using a powder X-ray diffraction (XRD) spectrum (Make: Rigaku Model: Smartlab, Japan). FT-IR (Fourier Transform Infra-red) spectrometer (Model: Spectrum Two, Made: Perkin Elmer) was used to identify the functional groups on the surface of the SWAC/ZrO_2-ZnO nanocomposite. The morphology and surface texture of the SWAC/ZrO_2-ZnO nanocomposite were studied using transmission electron microscopy (TEM) (Model: JEM-2100, Made: JEOL, JAPAN), BET surface area analyzer (Model: Autosorb iQ MP-AG (2 STAT) Anton Paar) was used to investigated the total surface area and total pore volume by N_2 adsorption-desorption isotherm studies along with the Barrett-Joyner-Halenda model (BJH) pore size distribution of activated carbon. (EDX) analysis for investigating elemental composition. Surface chemical states were investigated using XPS. A Horiba Fluoromax 8-4CP spectrofluorometer with a 150 W Xenon Lamp was used to study photoluminescence (PL) spectra. The zero-point charge (pH_{pzc}) of the SWAC/ZrO_2-ZnO nanocomposite samples was investigated using the batch equilibrium method [28].

5. Photocatalysis

The photocatalytic degradation of CPs was carried out with the use of an ultraviolet light-assisted photocatalytic device, and details of the photocatalysis experiments are described below.

5-1. Photocatalytic Device

In this work, photocatalytic degradation of CPs was carried out inside a photocatalytic reactor as described in the schematic diagram (Supplementary Fig. S1). On top of a magnetic stirrer, a 250 mL Pyrex glass jar containing 50 mL CPs solution was placed, and a dose of SWAC/ZrO_2-ZnO was stirred with the solution at the reactor's bottom. An ultraviolet light (mercury lamp, 450 W) with a maximum wavelength of 325 nm was placed 10 cm distance from the reaction mixture. A magnetic stirrer was installed directly under the double jacketed glass vessel to ensure that the reaction system was properly mixed. To keep the reactor temperature at 25 °C, a constant flow of water was employed throughout the reaction system. In addition, a reactor exhaust fan was installed to ensure that air was constantly circulated.

5-2. Photocatalytic Degradation

The photocatalytic degradation was performed by utilizing a continuous flow of water at room temperature throughout the reaction process. A stock solution of 1,000 ppm was first prepared by dissolving 1 g (5 mL of 20% of chlorpyrifos) of CPs in 1,000 ml double-distilled water. Furthermore, 100 ppm, 150 ppm, and 200 ppm were prepared by diluting the stock solution to the appropriate concentration. In the present work, the required amount of AC/ZrO_2-ZnO nanocomposite was dispersed in a 50 ml aqueous solution of varied CPs concentrations by vigorous stirring under dark conditions for 30 minutes to achieve adsorption-desorption equilibrium. Later, the UV light was switched on to start the photocatalytic reaction, and then after 10 minute intervals, 3 mL of sample was withdrawn and centrifuged for 10 minutes. The concentration of residual CPs was determined using a UV-Vis (PerkinElmer UV/Vis -365) spectrophotometer at λ_{max} of 221 nm. The following equation was used to calculate the degradation efficiency (R%) of CPs concentration.

$$R\% = \frac{C_o - C_e}{C_o} \times 100 \quad (1)$$

where, C_o (mg/L) is the initial concentration of CPs, and C_e (mg/L) is the equilibrium concentration of CPs.

6. Computational Studies

To further understand the reactivity of the SWAC/ZrO_2-ZnO nanocomposite, theoretical investigations using density functional theory (DFT) were performed. To investigate any potential interactions between the activated carbon surfaces and the ZrO_2-ZnO catalyst, an appropriate structure for the activated carbon surfaces must be designed. According to reports, the carbon surfaces are made up of graphite clusters with 12-25 carbon atoms (3-7 carbon rings) [26,29-31]. All the structures in this study were built using the Gauss View 05 software package, which was subsequently optimized using the Gaussian09 software. The computations were carried out by B3LYP (Beck's three-parameter hybrid, functional correlation of Lee-Yang-Parr hybrid functional method), 6-31G/LanL2DZ basis set in water with a dielectric constant (ε=80) to change the molecule geometry, lower the system's energy, and to achieve more stable conformation [32,33]. Quantum chemical parameters such as η (chemical hardness), H (HOMO-LUMO energy gap), μ (chemical potential), S (chemical softness), and ω (electrophilicity index) were used to comprehend the chemical reactivity of SWAC/ZrO_2-ZnO nanocomposite.

6-1. HOMO-LUMO Energy Gap

The chemical reactivity of a molecule is determined by the HOMO-LUMO energy gap (H); thus, a high value of the HOMO-LUMO energy gap signifies that the molecule is less reactive and more stable. Eq. (2) gives the HOMO-LUMO energy gap [34].

$$H = E_{LUMO} - E_{HOMO} \quad (2)$$

where E_{LUMO} represents the energy of the lowest unoccupied molecular orbital, whereas E_{HOMO} represents the energy of the highest occupied molecular orbital.

6-2. Chemical Hardness (η) and Chemical Softness (S)

The concepts of hardness (η) and softness (S) are important in understanding the behavior of chemical systems. The molecular stability increases as hardness increases and thereby its reactivity decreases. The chemical hardness (η) of a molecule is given by Eq. (3). The molecular stability increases as its softness decreases and thereby its reactivity increases. Eq. (4) gives the chemical softness (S) of a molecule [35].

$$\eta = \frac{E_{LUMO} - E_{HOMO}}{2} \quad (3)$$

$$S = \frac{1}{2\eta} \quad (4)$$

6-3. Chemical Potential and Electronegativity

The reactivity of a molecule is determined by chemical potential (μ) and electronegativity (X) which are represented by the Eqs. (5) and (6), respectively [36].

$$\mu = \frac{E_{HOMO} + E_{LUMO}}{2} \quad (5)$$

$$X = \frac{-(E_{HOMO} + E_{LUMO})}{2} \quad (6)$$

6-4. Electrophilicity Index

The electrophilicity index (ω) is a measurement of energy loss

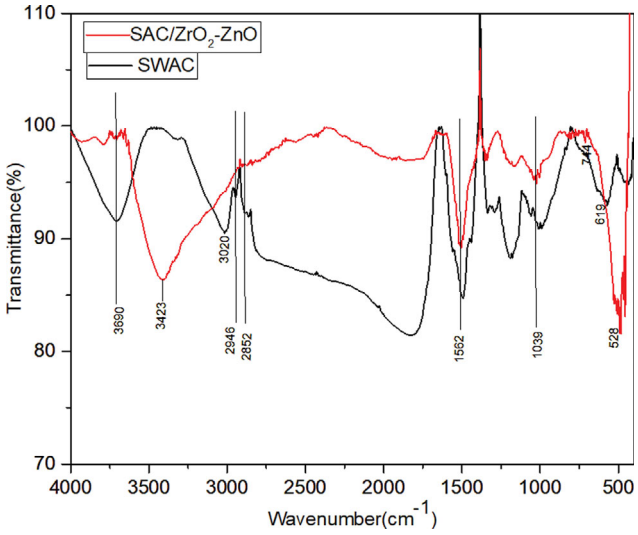

Fig. 1. FTIR spectra of SWAC/ZrO_2-ZnO nanocomposite.

caused by maximum electron flow between donor and acceptor. The higher the electrophilicity index, the molecule becomes more reactive. Electrophilicity index is calculated using Eq. (7) [37].

$$\omega = \frac{\mu^2}{2\eta} \tag{7}$$

when ω is greater than 1.5 eV, it has a high electrophilicity, ω less than 0.8 eV is considered marginal, and when ω is greater than 0.8 and less than 1.5 eV is considered moderate.

RESULTS AND DISCUSSION

1. Characterization of the Synthesized SWAC/ZrO_2-ZnO Nanocomposite

FTIR analysis confirmed the surface functionality of the SWAC/ZrO_2-ZnO nanocomposite (Fig. 1). From comparison with previous reports, the wide bands are similar compared to ACs obtained from many different biomass sources having functional groups [38-49]. Peaks at 3,432 cm^{-1} and 3,690 cm^{-1} have been ascribed to

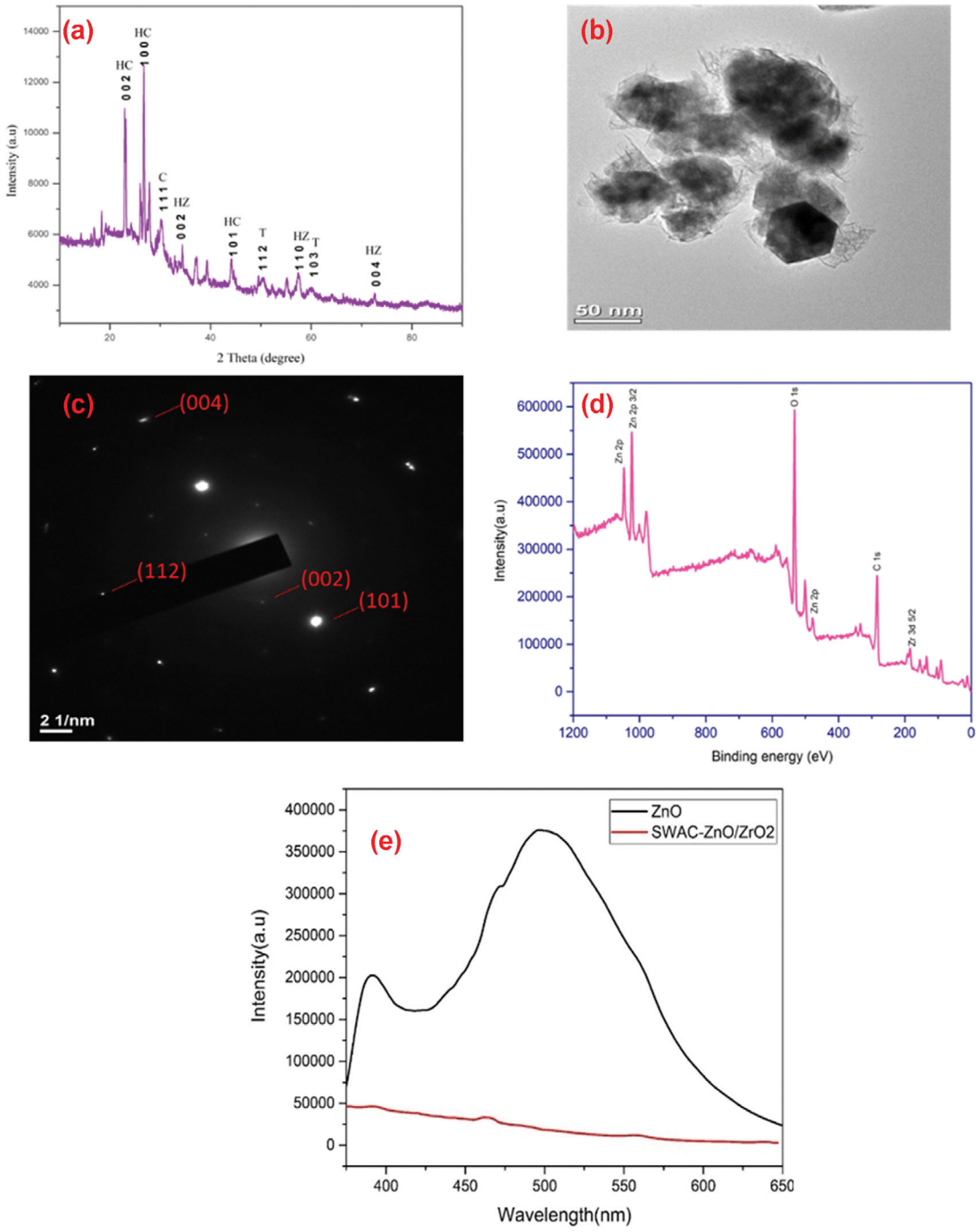

Fig. 2. (a) XRD, (HC- hexagonal phase of carbon, HZ-hexagonal phase of zincite and C, T-Cubic and Tetragonal phases of zirconia). (b) TEM, (c) SAED (d), XPS, and (e) Photoluminescence analyses of synthesized SWAC/ZrO_2-ZnO nanocomposite.

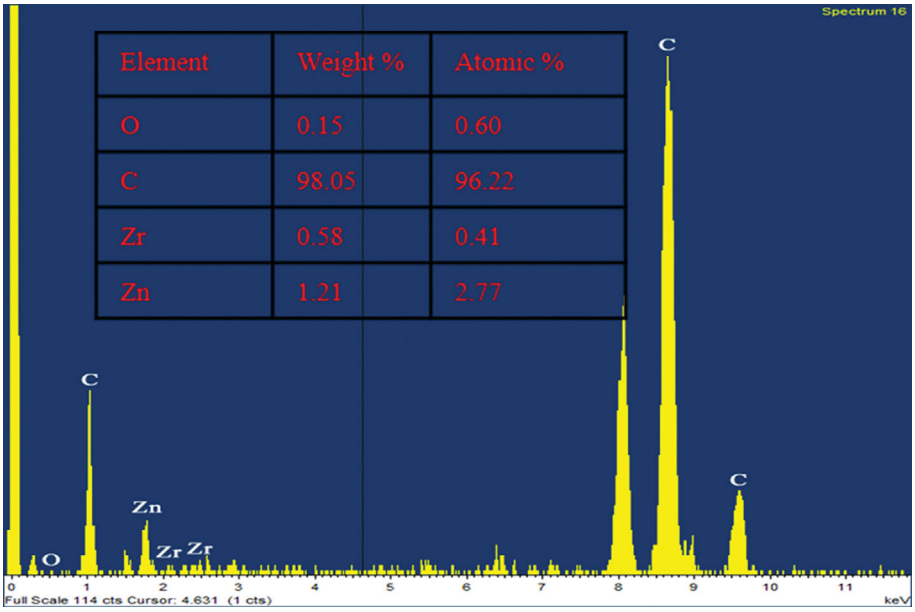

Fig. 3. EDX spectra of SWAC/ZrO_2-ZnO nanocomposite.

O-H stretching vibrations of water, alcohol, or carboxylic acid, and the band is comparable to previous reports [38,42-49]. The peaks at 3,020 cm^{-1} appear similar to previous findings and might be due to the presence of aromatic C-H stretch vibration [43,44]. Aliphatic C-H stretching vibration may be responsible for the bands at 2,946 cm^{-1} and 2,852 cm^{-1} having similar to those reported in earlier reports [38,43,45,48]. The presence of C-O stretch in alcohol, aldehyde, and carboxylic acid might explain the broad bands between 1,700 and 1,750 cm^{-1} that are similar to previous results [44-48]. The C=C aromatic peak was observed around 1,562 cm^{-1} [38,44-48]. The transmittance at 1,039 cm^{-1} and 1,208 cm^{-1} was attributed to C-O stretching in alcohol, carboxylic acid, phenol, ester, or ester group derivatives being similar to those reported in earlier reports [38,39,42-49]. The Zr-O vibrational mode is represented by the peak at 744 cm^{-1}. The Zn-O and Zn-O-Zr stretching vibrations are represented by the band at 528 cm^{-1} and 619 cm^{-1}, respectively [40,41].

The crystal structure of the synthesized SWAC/ZrO_2-ZnO nanocomposite was investigated using an XRD pattern, as shown in Fig. 2(a). The peak at 2θ=22.9° resembles the characteristic of disordered aromatic carbon structure with miller indices (0 0 2), the intensity peak at 2θ=~26°, and 44.17° corresponding to (1 0 0) and (1 0 1) planes of hexagonal graphitized carbon (JCPDS 00-025-0284). The presence of hexagonal zincite crystalline structure of ZnO is confirmed by the 2θ peaks at 34.43°, 57.16°, and 72.67°, with miller indices of (002), (110), and (004), respectively (JCPDS 01-075-1526). Furthermore, an X-ray diffractogram of commercial zirconia reveals the presence of a monoclinic phase, whereas an X-ray diffractogram of hydrothermally treated zirconia reveals cubic and tetragonal phases [50]. The ZrO_2 peaks were found at 2θ=30.1° corresponding to the cubic phase (111) (JCPDS 01-089-9069), 50.3°, and ~60° lattice planes (112), and (103) correlate to tetragonal ZrO_2 (JCPDS No. 01-079-1764). As a result, the Debye-Scherer equation was used to calculate the average crystalline size of SWAC/ZrO_2-ZnO nanocomposite, which was found to be ~39.41 nm.

TEM investigations revealed the presence of an amorphous SWAC/ZrO_2-ZnO-thick layer. Simultaneously, irregularly shaped nanoparticles with crystallites ranging in size from a few nanometers to several nanometers emerge on the surface of other particles as shown in Fig. 2(b) [51]. Thus, the particle size of synthesized SWAC/ZrO_2-ZnO was formed in the range of 21-44 nm.

The selected area electron diffraction (SAED) pattern as shown in Fig. 4(c) suggests that the material is polycrystalline. The defused character of the material indicates its decreased crystallinity, which is predicted owing to the integration of ZrO_2-ZnO nanocomposite particles inside the activated carbon envelop. The SAED patterns show spotty rings whose interplanar distances match with those of XRD crystal planes of hexagonal graphitized carbon (101), hexagonal zincite ZnO (002), and (004), and tetragonal ZrO_2 (112) as shown in Fig. 3(a) [22,52].

XPS analysis was used to ascertain the chemical state of C, O, Zn and Zr contained on the surface of synthesized SWAC/ZrO_2-ZnO nanocomposite. As shown in Fig. 2(c), C, O, Zn, and Zr elements coexist on the nanocomposite's surface, with matching peaks at 284 eV (C 1s), 532 eV (O 1s), 1,024 eV (Zn 2p 3/2), 1,044 eV, (Zn 2p) and 184 eV (Zr 3d), respectively. The XPS spectra suggested the formation of a SWAC/ZrO_2-ZnO nanocomposite [53,54].

Fig. 2(d) shows the PL (Photoluminescence) spectra of pure ZnO and the synthesized SWAC/ZrO_2-ZnO composite. The recombination of electron hole pairs and the emission of photons are involved in photoluminescence. As photocatalytic efficiency increases, photoluminescence intensity and electron hole recombination efficiency decrease [21,55]. As seen in Fig. 2(e), ZnO has the highest PL intensity, suggesting the highest rate of electron-hole recombination. The PL intensity reduces after the formation of the SWAC/ZrO_2-ZnO nanocomposite, showing that the electron-hole recombination rate lowers, implying that the SWAC/ZrO_2-ZnO nanocomposite has higher photocatalytic efficiency.

EDX was used to further investigate the elemental composition of the prepared SWAC/ZrO_2-ZnO nanocomposite (Fig. 3). The EDX graph reveals that the prepared SWAC/ZrO_2-ZnO nanocomposite contains 98.05% carbon, 0.15% oxygen, 0.58% Zr and 1.21% Zn. The presence of C, O, Zr and Zn peaks in the EDX graph is due to the use of carbon, zirconium dioxide and Zinc acetate in the preparation of the SWAC/ZrO_2-ZnO nanocomposite.

To investigate the surface area and porosity of the SWAC/ZrO_2-

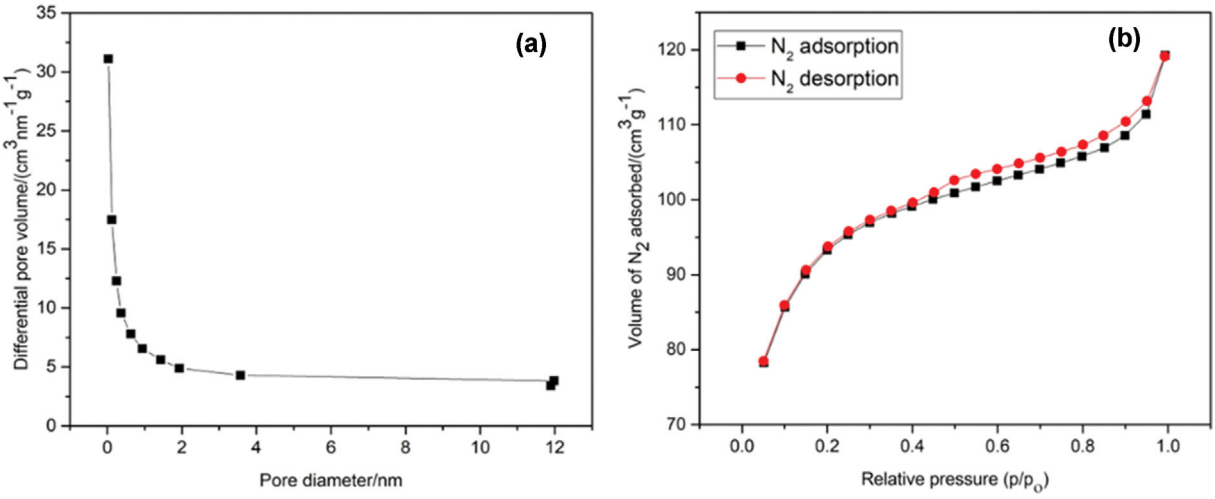

Fig. 4. (a) Pore size distribution and (b) N_2 adsorption-desorption isotherm studies of SWAC/ZrO_2-ZnO nanocomposite.

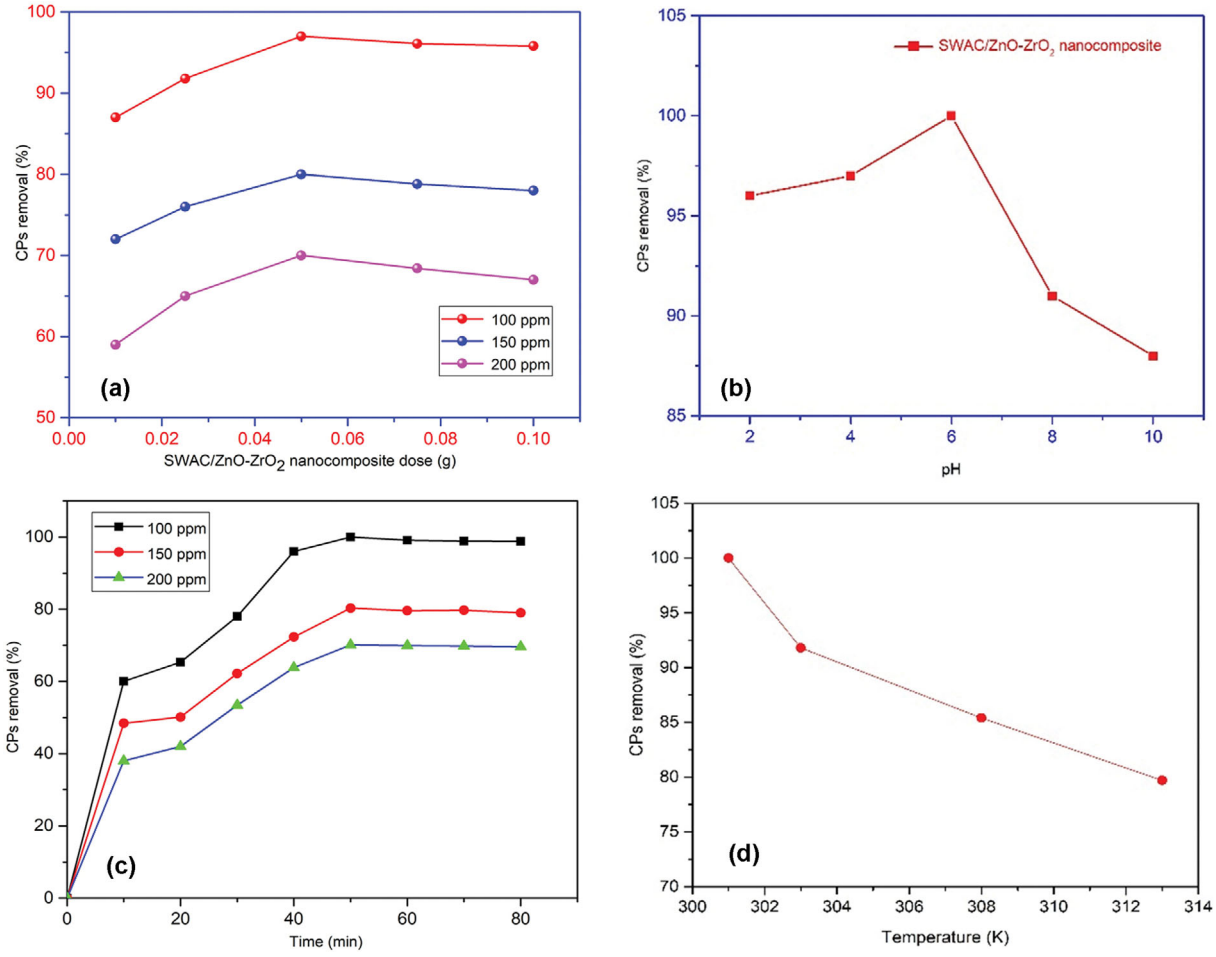

Fig. 5. (a) Effect of SWAC/ZrO_2-ZnO Nanocomposite dosage, (b) Effect of pH, and (c) Effect of Initial CPs Concentration and light irradiation time, (d) Effect of Temperature in the degradation of CPs solution.

ZnO nanocomposite, N_2 adsorption-desorption isotherm studies were performed along with the Barrett-Joyner-Halenda model (BJH) pore size distribution. The N_2 adsorption-desorption isotherm of the SWAC/ZrO_2-ZnO nanocomposite is depicted in Fig. 4(b). It presents a physisorption isotherm of type I and IV. The presence of micropores in the SWAC/ZrO_2-ZnO sample is demonstrated by a high adsorption limit at low relative pressure (p/p_o 0.99). The formation of a large number of mesopores in the SWAC/ZrO_2-ZnO nanocomposite is demonstrated by the H4 type hysteresis loop at a relative pressure p/p_o range of 0.4 to 1.0, which results from mesopores filling and emptying by capillary condensation. SWAC/ZrO_2-ZnO nanocomposite has a BET surface area of 223.387 m^2g^{-1} and a total pore volume of 0.1845 cm^3g^{-1}. From the desorption branches of the isotherms, the pore size distributions are calculated using the BHJ as shown in Fig. 4(a), the pore size distribution of SWAC/ZrO_2-ZnO is primarily narrow, with an average diameter of 3.81 nm.

2. Photocatalytic Activity

2-1. Effect of SWAC/ZrO_2-ZnO Nanocomposite Dosage

The photocatalytic activity of the synthesized SWAC/ZrO_2-ZnO nanocomposite for the degradation of CPs solutions was investigated at various doses (0.01-0.10 g) and for various concentrations (100 ppm, 150 ppm, and 200 ppm). For all CPs concentrations, the percentage of CPs degradation increased with the increase of nanocomposite doses till 0.05 g (Fig. 5(a)). Under UV light irradiation for 50 minutes, the maximum percentage of degradation (97%) was achieved for 100 ppm CPs concentration at the dosage of 0.05 g SWAC/ZrO_2-ZnO nanocomposite.

As the catalyst loading increases, the number of active sites in the solution increases, while ultra-violet light penetration reduces due to the high particle concentration, resulting in lower CPs degradation. Similar studies on other catalysts have been reported in the literature [8,56,57]. Thus, for further studies, 0.05 g of the SWAC/ZrO_2-ZnO nanocomposite was taken to be the optimal dosage for CPs degradation process.

2-2. Effect of pH on CPs Concentration

To determine the optimal pH for CPs degradation, an experiment was carried out at different pH ranges from 2 to 10 with an initial CPs concentration of 100 ppm, nanocomposite dose of 0.05 g, UV light irradiation time of 50 mins, and temperature of 298 K. Fig. 5(b) shows the photodegradation of CPs increases with an increase in pH from 2 to 6 and decreases thereafter in a basic medium. The pH_{zpc} (zero point charge) of SWAC/ZrO_2-ZnO nanocomposite was found to be 6.8, which signifies that the surface of the SWAC/ZrO_2-ZnO nanocomposite is negatively charged above this pH and positively charged below this pH. Therefore, at lower pH, a positively charged photocatalyst surface is likely to have a higher electrostatic attraction affinity towards oppositely charged CPs solution. In basic conditions, hydroxyl radicals behave as weak acids, forming less reactive ^-O ions upon reaction with ^-OH ions. Furthermore, at basic pH, the breakdown of H_2O_2 to H_2O and O_2 occurs more quickly, resulting in decreased photocatalytic activity. Similar studies on other catalysts have been reported in the literature [9,57,58]. As a result, the optimal pH for CPs photodegradation was found to be pH 6.0.

2-3. Effect of Initial CPs Concentration and Light Irradiation Time

The effect of initial concentration on the rate of CPs degradation was studied at varied CPs concentrations (100, 150, and 200 ppm) at the optimal dosage of 0.05 g SWAC/ZrO_2-ZnO nanocomposite and pH=6). A graph of CPs removal % vs time is shown in Fig. 5(c). After 50 minutes of UV light irradiation, 100% degradation of CPs was observed for a 100 ppm solution. On the other hand, the removal percentage for 150 ppm and 200 ppm concentrations of CPs, was reduced to 80 percent and 70 percent, respectively. As a result, for all subsequent experiments, the optimal concentration is determined to be 100 ppm.

In addition, the lesser availability of hydroxyl radical species in the reaction media might explain why the CPs degrades more slowly. Photocatalytic degradation is started by reactive hydroxyl radicals produced as a result of light exposure, and the degradation process occurs mostly on the nanocomposite's surface. When the CPs concentration increases, light particles become trapped between the CPs particles and are unable to reach the nanocomposite surface [55]. As a result, the formation of reactive hydroxyl radicals decreases and the breakdown of CPs decreases.

2-4. Effect of Temperature

The effect of temperature on the degradation of CPs was examined at 301, 303, 308, and 311 K while maintaining the other parameters constant (dosage of 0.05 g SWAC/ZrO_2-ZnO nanocomposite, 100 ppm CPs solution, and pH=6 for 50 minutes). Fig. 5(d) depicts a plot of percentage removal of CPs vs temperature. It was observed that with increases in temperature the removal percentage of CPs decreased [59].

3. LC-MS Analysis of CPs Degradation

LC-MS spectra (Make: INKAR, Model: Expression-S) is utilized to identify the degraded products after the photocatalytic reaction. Fig. 6 represents the spectra of the reaction mixture after 50 mins of UV irradiation. Based on the detected components from mass spectra, an effort made to understand the degradation process in detail shows the product obtained given in the Table S2 (Supplementary Table S2). The decomposition process of CPs proceeds in

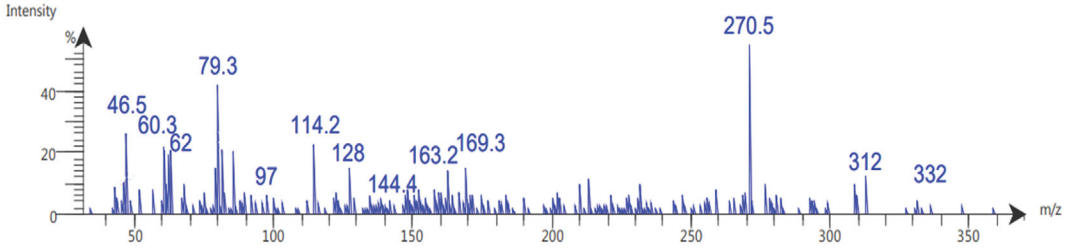

Fig. 6. LC-MS spectra of the photolytic degradation products of CPs.

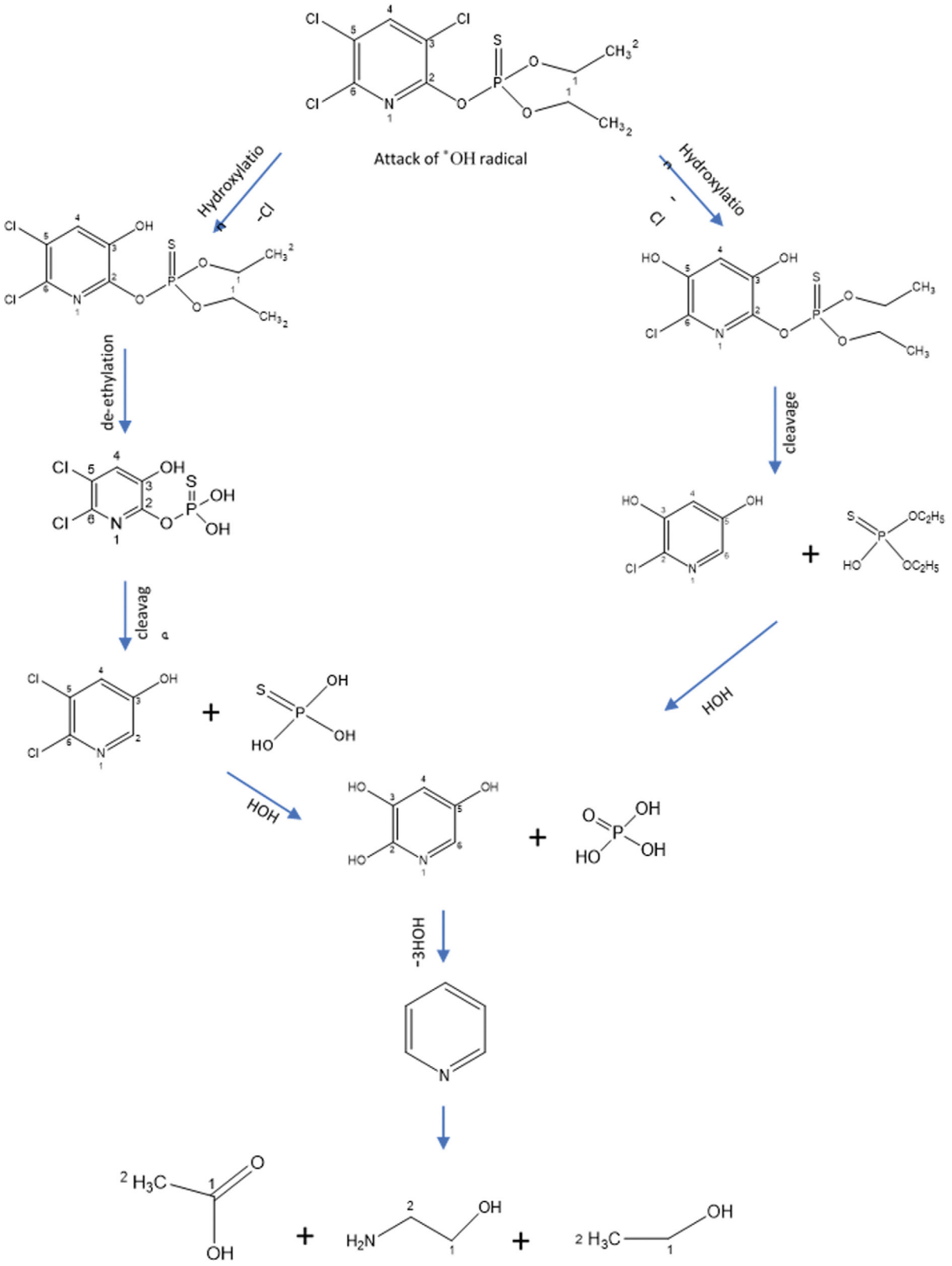

Scheme 1. Photocatalytic degradation pathways of CPs using SWAC/ZrO_2-ZnO nanocomposite.

a similar way as reported in the literature [8,60]. Photodegradation occurs via a free radical process, and the possible mechanism is illustrated in Scheme 1.

4. Photodegradation Kinetics of Chlorpyrifos

The kinetic studies were carried out at optimum conditions, i.e., with 100 ppm CPs solutions (50 ml), pH at 6, irradiation time of

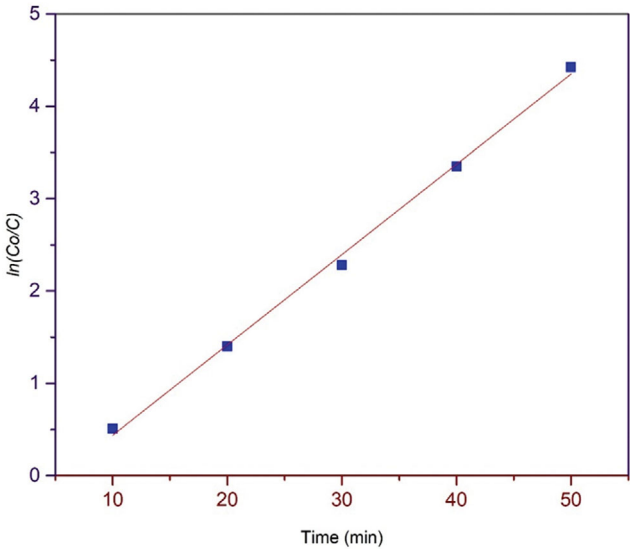

Fig. 7. Pseudo-first-order rate kinetics of CPs degradation loaded on SWAC/ZrO_2-ZnO nanocomposite.

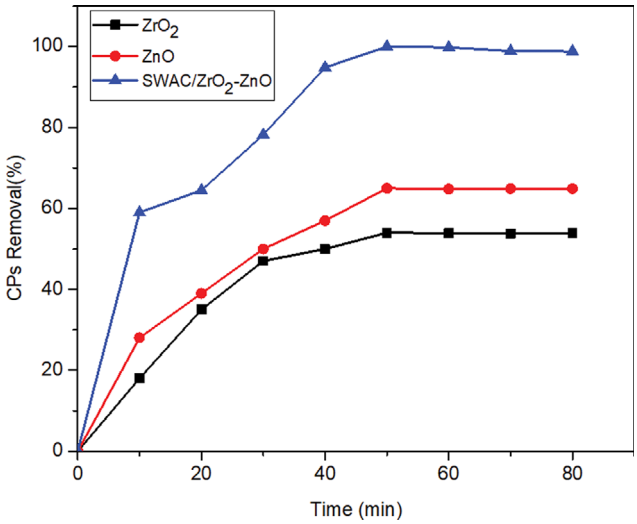

Fig. 8. Photocatalytic activity test of CPs degradation by ZrO_2, ZnO and synthesized SWAC/ZrO_2-ZnO nanocomposite.

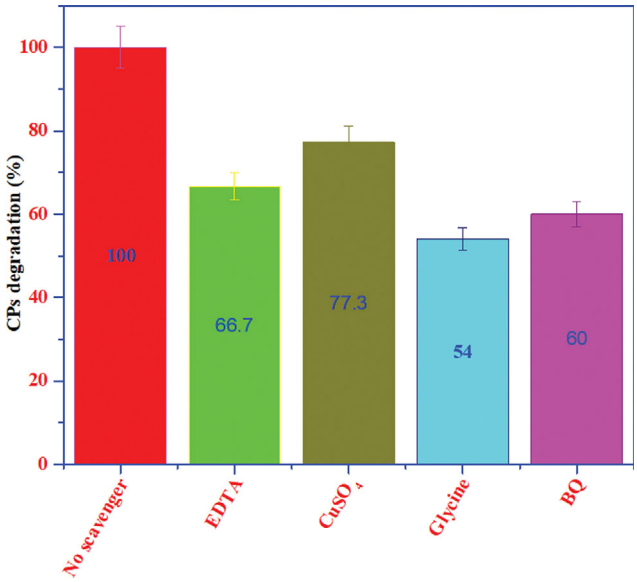

Fig. 9. Photocatalytic degradation of CPs in the presence of different scavengers using SWAC/ZrO_2-ZnO nanocomposite.

50 mins, and 0.05 g of SWAC/ZnO-ZrO_2 nanocomposite. The photocatalytic performance of the CPs concentration was determined by employing the Langmuir-Hinshelwood model [60]. The kinetics study was described using pseudo first-order rate and the half-life period. The equations are given as follows.

$$\ln(Co/C) = k_{ap}t \quad (8)$$

$$t_{1/2} = \frac{\ln 2}{k_{ap}} \quad (9)$$

where Co denotes the CPs initial concentration, C denotes the concentration at time t, K_{ap} denotes the apparent reaction rate constant, and $t_{1/2}$ denotes the half-life period.

For the SWAC/ZrO_2-ZnO nanocomposite, the linear plot of ln(Co/C) vs time shows a strong correlation coefficient (R^2 value: 0.99), indicating that the CPs degradation follows pseudo-first-order rate kinetics (Fig. 7). The photocatalytic rate constant (K_{ap}) value was derived from the slope of the curve to be 0.09778 min^{-1} and $t_{1/2}$ was calculated using Eq. (12) to be 7.088 mins.

5. Catalyst Efficiency for the Degradation of CPs

The experiment was performed using different catalysts, such as pristine ZrO_2, pristine ZnO, and prepared SWAC/ZrO_2-ZnO nanocomposite, while maintaining all other parameters at optimum condition (dose of 0.05 g, initial CPs concentration of 100 ppm, and UV light irradiation time of 50 minutes). In all situations, the prepared SWAC/ZrO_2-ZnO nanocomposite catalysts surpass the pristine catalysts in terms of photocatalytic activity towards CPs degradation (Fig. 8). The decreasing order of photocatalytic efficiency towards CPs degradation is as follows: prepared SWAC/ZrO_2-ZnO (100%)>pristine ZnO (65%)>pristine ZrO_2 (54%). This suggests that photocatalytic activity improved after ZnO was doped with ZrO_2 supported by activated carbon.

6. Effect of Radical Scavengers on Photocatalytic Degradation of CPs

The type and amount of reactive oxidation species produced by photo-generated electrons and holes are closely related to photocatalytic activity. Four scavengers were used to explore the reactive species in the photocatalytic reaction process to further detect the main reactive oxidative species in the photocatalytic process for elucidating the photocatalytic mechanism. Scavengers for hydroxyl radicals (*OH), holes (h^+), superoxide radicals ($*O^{2-}$), and electrons (e^-) were glycine, EDTA, BQ (p-benzoquinone), and $CuSO_4$ in this experiment. As demonstrated in Fig. 9, the percentage removal decreases from 100% to 54.0% (Glycine), 66.7% (EDTA), 77.3% ($CuSO_4$), and 60.0% (BQ). The addition of four types of scavengers significantly reduces the photodegradation efficiency of the SWAC/ZrO_2-ZnO nanocomposite, indicating that $*O^{2-}$, h^+, e^- and *OH may be the active species on the CPs degradation in the system. More importantly, the promoting effect of these reactive oxi-

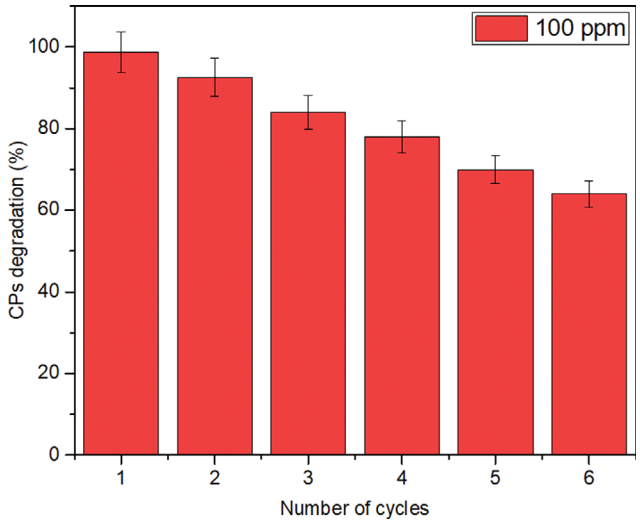

Fig. 10. CPs degradation efficiency of SWAC/ZrO_2-ZnO nanocomposite up to six cycles.

dation species decreases in the following order: hydroxyl radical (*OH)>superoxide radical ($*O^{2-}$)>hole (h^+)>electron (e^-). These findings clearly show that the most important reactive oxidation species, *OH, h^+, e^- and $*O^{2-}$, are significantly increased in the SWAC/ZrO_2-ZnO nanocomposite.

7. Nanocomposite Reusability and Photostability

The reusability of the produced nanocomposite for photocatalytic CPs degradation was tested for six cycles. To reuse the nanocomposite, the nanocomposite remaining in the reaction medium was separated by centrifuging the solution after each photocatalytic reaction. The nanocomposite was then washed with double distilled water and oven dried. The dried nanocomposite was then employed for photocatalytic CPs degradation (Fig. 10). The CPs degradation rate in the first cycle was 100%, which decreased to 92.60% in the second cycle, 88% in the third cycle, 83% in the fourth cycle and for the fifth cycle it degraded up to 74%. With increasing usage, the degrading efficiency of the nanocomposite decreased significantly. This decrease in degradation efficiency might be attributed to a decrease in unoccupied adsorption sites on SWAC/ZrO_2-ZnO nanocomposite for CPs adsorption. It might also be owing to the release of photoactive substances from the SWAC/ZrO_2-ZnO nanocomposite during the recycling process [56]. The degradation efficiency of the nanocomposite was found to be approximately 68% in the sixth cycle, indicating that the SWAC/ZrO_2-ZnO nanocomposite still has outstanding utilization capacity after numerous cycles.

Table 1. Show the energy gap of different catalysts

System	Energy gap (eV)	Reference
SWAC/ZrO_2-ZnO	0.02364	Present case
ZnBTC	2.3004	[62]
$Mg(H_2BTC)_2(H_2O)_2$	3.57	[63]
TiO_2-NP/PAC composite	0.02501	[23]
SWCNTs	1.16	[64]

8. Computational Studies

Theoretical investigation was used to gain insight into the reactivity of SWAC/ZrO_2-ZnO nanocomposite. For the current study, four fused benzene ring configurations were used to model SWAC [61]. SWAC was coupled with ZrO_2-ZnO through the formation of hydrogen bonding via O-linkage of the O-Zr-O bond in SWAC/ZrO_2-ZnO nanocomposite. The optimized molecular structures of ZrO_2-ZnO and SWAC/ZrO_2-ZnO composite, as well as their HOMO and LUMO structures, are shown in Fig. 11.

Table S3 (Supplementary Table S3) shows the quantum chemical descriptors and calculated values of ZrO_2-ZnO and SWAC/ZrO_2-ZnO nanocomposite, including HOMO-LUMO band gap energies, ionization potentials, and dipole moment. The dipole moment increases from 19.0179 to 37.2082 Debye and the energy gap decreases from 0.05745 to 0.02364 eV when ZrO_2-ZnO is introduced into SWAC, as shown in the table. These modifications imply that the nanocomposite material produced is extremely reactive

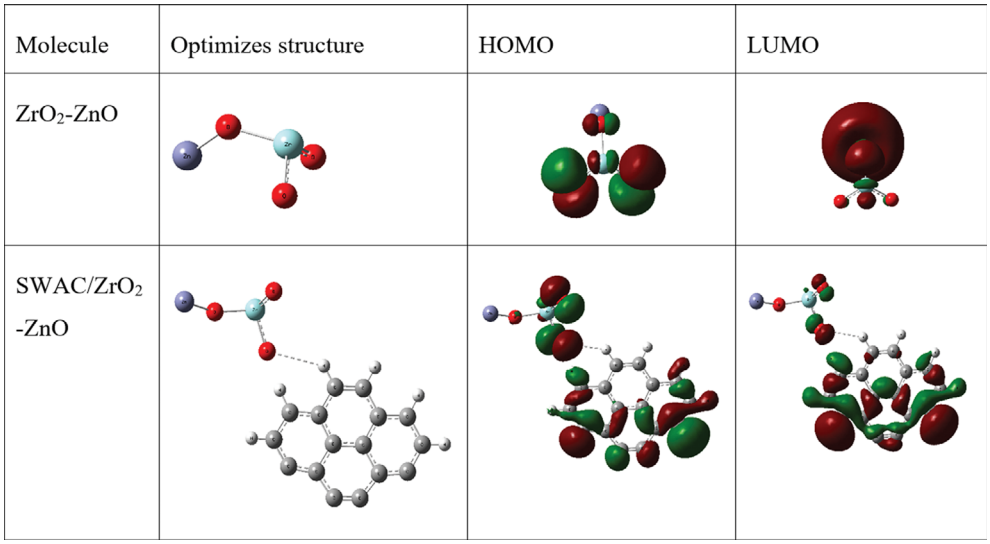

Fig. 11. HOMO and LUMO molecular orbital of ZrO_2-ZnO and SWAC/ZrO_2-ZnO nanocomposite.

Table 2. Molecular chemical descriptors of ZrO_2-ZnO and SWAC/ZrO_2-ZnO nanocomposite

System	η (eV)	S (eV)	μ (eV)	ω (eV)	X (eV)
ZrO_2-ZnO	0.028725	14.406	−0.11394	0.0009	0.11394
SWAC/ZrO_2-ZnO	0.01182	42.301	−0.17992	1.3693	0.17992

Table 3. Comparative study of Chlorpyrifos removal percentage (%) with other nanocomposite materials

Organic pollutant	Nanocomposite materials	Removal percentage (%)	Reference
Chlorpyrifos	SWAC/ZrO_2-ZnOnanocomposite	100	Present case
	CFGO/ZnO nanorod composite	99.4	[65]
	CuO/TiO_2/PANI nanocomposite	95	[57]
	CeO_2/TiO_2/SiO_2 nanocatalyst	90.8	[58]
	Fe: ZnO nanocomposite	93.5	[66]
	ZnS nanoparticles	85.29	[67]
	TiO_2/H_2O_2	74.38	[68]
	$CoFe_2O_4$@TiO_2/rGO nanocatalyst	89.9	[11]
	CuS/BSC heterojunction system	>95%	[69]

and has a favorable interaction.

The HOMO-LUMO band gap energies of SWAC/ZrO_2-ZnO nanocomposite are compared to those of other Catalysts described in the literature in Table 1. According to the table, the HOMO-LUMO band gap energies of SWAC/ZrO_2-ZnO nanocomposite have a lower energy gap than other catalysts. As a result of these modifications, the nanocomposite material formed is extremely reactive and has a favorable interaction.

The molecular chemical descriptors of ZrO_2-ZnO and SWAC/ZrO_2-ZnO nanocomposite are shown in Table 2. The chemical hardness (η) of SWAC/ZrO_2-ZnO was found to be lower than that of ZrO_2-ZnO. Moreover, The chemical softness (S) of SWAC/ZrO_2-ZnO nanocomposite is greater than ZrO_2-ZnO, indicating that SWAC/ZrO_2-ZnO nanocomposite has a higher reactivity than ZrO_2-ZnO [3]. These results signify that by doping ZrO_2-ZnO nanoparticles into activated carbon, the reactivity of the nanocomposite increases. Also, SWAC/ZrO_2-ZnO has greater electronegativity value (X=0.17992 eV) and electrophilicity index (ω=1.3693 eV) than ZrO_2-ZnO (X=0.11394 eV, ω=0.0009 eV) suggesting that it is a better electron acceptor. Moreover, the μ value of the SWAC/ZrO_2-ZnO nanocomposite is lower than that of ZrO_2-ZnO, indicating that it is easier to gain electrons rather than to lose an electron.

As a result of this computational work, it is clear that incorporating ZrO_2-ZnO into SWAC improves its reactivity, which increases its effectiveness in removing CPs. Thus, these theoretical investigations help in the selection of highly effective materials for pollution removal by providing a theoretical concept of the reactivity of the materials.

9. Comparative Study of SWAC/ZrO_2-ZnO Nanocomposite with other Nanocomposite Materials

Table 3 presents a comparative study of SWAC/ZrO_2-ZnO nanocomposite with other nanocomposite materials described in the literature to comprehend the degradation efficiency of CPs. This suggests that the SWAC/ZrO_2-ZnO nanocomposite has a relatively high activity under ideal circumstances and is a viable photocatalyst for the removal of CPs in water.

CONCLUSIONS

A novel SWAC/ZrO_2-ZnO nanocomposite was developed by effectively immobilizing a ZrO_2-ZnO photocatalyst on SWAC using a hydrothermal technique. FTIR, XRD, TEM-SEAD, XPS, LC-MS, and PL instruments were used to characterize SWAC/ZrO_2-ZnO nanocomposite. The XRD analysis showed that the SWAC/ZrO_2-ZnO nanocomposite crystal size was found to be 39.41 nm. The LC-MS analysis revealed that the CPs molecule had been fragmented into smaller m/z ratios. The insecticide chlorpyrifos (100 ppm) was degraded (100%) with a 0.05 g dose of SWAC/ZrO_2-ZnO nanocomposite under UV light irradiation for 50 mins at pH 6. SWAC/ZrO_2-ZnO nanocomposite photodegradation of CPs follows pseudo-first-order kinetics. Density functional theory (DFT) simulations also revealed the formation of hydrogen bonding via O-linkage of the O-Zr-O bond with SWAC to form chemically reactive SWAC/ZrO_2-ZnO nanocomposite. Thus, the SWAC/ZrO_2-ZnO nanocomposite could serve as a promising photocatalyst for the degradation of chlorpyrifos from an aqueous solution.

ACKNOWLEDGEMENTS

The Authors Soremo L Ezung, Mridushmita Baruah, and Shisak Sharma are grateful to University Grants Commission, New Delhi for the UGC Non-NET fellowship (PF/RDC/NNF-72/2018-2912, PF/RDC/NNF-41/2017-1521, and NU/RDC/NNF-82/2020-928). Suraj Kumar acknowledges the financial assistance from the Department of Science and Technology as INSPIRE Fellowship (IF190895). Support under DST-FIST (No. SR/FST/CSI-276/2016(C)) is also acknowledged.

SUPPORTING INFORMATION

Additional information as noted in the text. This information is available via the Internet at http://www.springer.com/chemistry/journal/11814.

REFERENCES

1. S. Das and T. K. Adhya, *J. Environ. Manage.*, **152**, 36 (2015).
2. Z. Chishti, S. Hussain, K. R. Arshad, A. Khalid and M. Arshad, *J. Environ. Manage.*, **114**, 372 (2013).
3. Y. Samet, L. Agengui and R. Abdelhédi, *Chem. Eng. J.*, **161**, 167 (2010).
4. M. N. Mori, H. Oikawa, M. H. O. Sampa and C. L. Duarte, *J. Radioanal. Nucl. Chem.*, **270**, 99 (2006).
5. K. Maya, R. S. Singh, S. N. Upadhyay and S. K. Dubey, *Process Biochem.*, **46**, 2130 (2011).
6. M. M. Jacob, M. Ponnuchamy, A. Kapoor and P. Sivaraman, *J. Environ. Chem. Eng.*, **8** 103904 (2020).
7. M. Samy, M. G. Ibrahim, M. Gar Alalm, M. Fujii, K. E. Diab and M. ElKady, *Chem. Eng. J.*, **395**, 124974 (2020).
8. D. Pathania, A. Sharma, S. Kumar, A. K. Srivastava and A. Kumar, *Chemosphere*, **277**, 130315 (2021).
9. E. S. Agorku, A. T. Kuvarega, B. B. Mamba, A. C. Pandey and A. K. Mishra, *J. Rare Earths*, **33**, 498 (2015).
10. E. D. Sherly, J. J. Vijaya, N. C. S. Selvam and L. J. Kennedy, *Ceram. Int.*, **40**, 5681 (2014).
11. V. K. Gupta, D. Pathania, P. Singh, B. S. Rathore and P. Chauhan, *Carbohydr. Polym.*, **95**, 434 (2013).
12. T. A. Saleh, M. A. Gondal, Q. A. Drmosh, Z. H. Yamani and A. ALyamani, *Chem. Eng. J.*, **166**, 407 (2011).
13. O. Benton, S. Apollo, B. Naidoo and A. Ochieng, *Chem. Eng. Commun.*, **203**, 1443 (2016).
14. H. Anwer and J. W. Park, *J. Hazard. Mater.*, **358**, 416 (2018).
15. A. I. Vaizoğullar, *Mater. Technol.*, **34**, 433 (2019).
16. H. F. Wu, C. C. Lin and P. Shen, *J. Non-Cryst. Solids*, **209**, 76 (1997).
17. P. Muthirulan, M. Meenakshisundararam and N. Kannan, *J. Adv. Res.*, **4**, 479 (2013).
18. M. Zbair, Z. Anfar, H. A. Ahsaine, N. El Alem and M. Ezahri, *J. Environ. Manage.*, **206**, 383 (2018).
19. X. Chen, X. Xu, J. Cui, C. Chen, X. Zhu, D. Sun and J. Qian, *J. Hazard. Mater.*, **392**, 122331 (2020).
20. J. Matos, J. Laine and J. M. Herrmann, *J. Catal.*, **200**, 10 (2001).
21. M. Baruah, S. L. Ezung, A. Supong, P. C. Bhomick, S. Kumar and D. Sinha, *Korean J. Chem. Eng.*, **38**, 1277 (2021).
22. D. Mohanta and M. Ahmaruzzaman, *J. Environ. Chem. Eng.*, **6**, 356 (2018).
23. M. Baruah, A. Supong, P. Chandra, B. Rituparna and K. Chubaakum, *Nanotechnol. Environ. Eng.*, **5**, 1 (2020).
24. T. N. V. de Souza, S. M. L. de Carvalho, M. G. A. Vieira, M. G. C. da Silva and D. D. S. B. Brasil, *Appl. Surf. Sci.*, **448**, 662 (2018).
25. H. Ullah, A. A. Tahir and T. K. Mallick, *Sens. Actuators, B Chem.*, **241**, 1161 (2017).
26. A. Supong, P. C. Bhomick, M. Baruah, C. Pongener, U. B. Sinha and D. Sinha, *Sustain. Chem. Pharm.*, **13**, 100159 (2019).
27. A. Shokufeh, *Res. J. Chem. Environ.*, **19**, 28 (2015).
28. P. C. C. Faria, J. J. M. Órfão and M. F. R. Pereira, *Water Res.*, **38**, 2043 (2004).
29. B. Padak and J. Wilcox, *Carbon*, **47**, 2855 (2009).
30. L. R. Radovic, *Carbon*, **43**, 907 (2005).
31. J. R. Pliego, S. M. Resende and E. Humeres, *Chem. Phys.*, **314**, 127 (2005).
32. S. L. Ezung, M. Baruah, A. Supong, S. Sharma and D. Sinha, *Sustain. Chem. Pharm.*, **26**, 100643 (2022).
33. S. Kumar, S. Sharma, R. Karmaker and D. Sinha, *Mater. Today Commun.*, **26**, 101755 (2021).
34. G. Q. Blantocas, A. S. Alaboodi and H. M. Abdel-baset, *Arab. J. Sci. Eng.*, **43**, 389 (2018).
35. A. Bendjeddou, T. Abbaz, A. K. Gouasmia and D. Villemin, *Int. Res. J. Pure Appl. Chem.*, **12**, 1 (2016).
36. A. Bendjeddou, T. Abbaz, S. Maache, R. Rehamnia, A. K. Gouasmia and D. Villemin, *Rasayan J. Chem.*, **6**, 32 (2016).
37. S. Pratihar and S. Roy, *J. Org. Chem.*, **75**, 4957 (2010).
38. A. Supong, P. C. Bhomick, U. B. Sinha and D. Sinha, *Korean J. Chem. Eng.*, **36**, 2023 (2019).
39. D. Angin, *Fuel*, **115**, 804 (2014).
40. M. M. Ibrahim, *Spectrochim. Acta A.*, **145**, 487 (2015).
41. M. Obaidullah, T. Furusawa, I. A. Siddiquey, N. M. Bahadur, M. Sato and N. Suzuki, *Adv. Powder Technol.*, **29**, 1804 (2018).
42. N. Nasseh, F. S. Arghavan, S. Rodriguez-Couto, A. H. Panahi, M. Esmati and T. J. A-Musawi *Adv. Powder Technol.*, **31**, 875 (2020).
43. L. Gao and Y. Wei, *J. Sep. Sci.*, **39**, 3186 (2016).
44. S. Joshi and B. P. Pokharel, *J. Inst. Eng.*, **9**, 79 (2013).
45. X. Liu, C. He, X. Yu, Y. Bai, L. Ye, B. Wang and L. Zhang, *Powder Technol.*, **326**, 181 (2018).
46. I. I. Gurten, M. Ozmak, E. Yagmur and Z. Aktas, *Biomass Bioenergy*, **37**, 73 (2012).
47. A. Allwar, *J. Appl. Chem.*, **2**, 9 (2012).
48. D. Krishnaiah, C. G. Joseph, S. M. Anisuzzaman, W. M. A. W. Daud, M. Sundang and Y. C. Leow, *Korean J. Chem. Eng.*, **34**, 1377 (2017).
49. P. C. Bhomick, A. Supong, M. Baruah and C. Pongener, *Sustain. Chem. Pharm.*, **10**, 41 (2018).
50. A. Behbahani, S. Rowshanzamir and A. Esmaeilifar, *Procedia Eng.*, **42**, 908 (2012).
51. O. Długosz, K. Szostak and M. Banach, *Appl. Nanosci.*, **10**, 941 (2020).
52. A. Quintana, A. Altube, E. García-Lecina, S. Suriñach, M. D. Baró, J. Sort, E. Pellicer and M. Guerrero, *J. Mater. Sci.*, **52**, 13779 (2017).
53. K. Mishra, S. H. Kim and Y. R. Lee, *ChemSusChem*, **12**, 881 (2019).
54. S. B. Khan, K. A. Alamry, H. M. Marwani, A. M. Asiri and M. M. Rahman, *Compos. Part B Eng.*, **50**, 253 (2013).
55. R. Shen, J. Xie, P. Guo, L. Chen, X. Chen and X. Li, *ACS Appl. Energy Mater.*, **1**, 2232 (2018).
56. M. Baruah, S. L. Ezung, S. Sharma, U. B. Sinha and D. Sinha, *Inorg. Chem. Commun.*, **144**, 109905 (2022).
57. R. Nekooie, T. Shamspur and A. Mostafavi, *J. Photochem. Photobiol. A Chem.*, **407**, 113038 (2021).
58. R. Mansourian, S. M. Mousavi, S. Alizadeh and S. Sabbaghi, *Can. J. Chem. Eng.*, **100**, 451 (2022).
59. M. M. Jacob, M. Ponnuchamy, A. Kapoor and P. Sivaraman, *J. Environ. Chem. Eng.*, **8**, 103904 (2020).
60. A. Saljooqi, T. Shamspur and A. Mostafavi, *Environ. Sci. Pollut. Res.*, **28**, 9146 (2021).
61. P. He, J. Wu, X. Jiang, W. Pan and J. Ren, *Appl. Surf. Sci.*, **258**, 8853 (2012).
62. C. A. Anyama, B. I. Ita, A. A. Ayi, H. Louis, E. E. D. Okon, J. O. Ogar and C. O. Oseghale, *ACS Omega*, **6**, 28967 (2021).
63. E. E. Ekpenyong, H. Louis, C. A. Anyama, J. O. Ogar, P. M. Utsu and

A. A. Ayi, *J. Mol. Struct.*, **1220**, 128641 (2020).
64. M. A. Daiem, A. A. Alotaibi, E. M. Alosime, B. Zaidi and N. Said, *Pol. J. Environ. Stud.*, **29**, 3535 (2020).
65. T. S. Anirudhan, F. Shainy, V. C. Sekhar and V. S. Athira, *J. Photochem. Photobiol. A Chem.*, **418**, 113333 (2021).
66. S. H. Khan, B. Pathak and M. H. Fulekar, *Nanotechnol. Environ. Eng.*, **3**, 13 (2018).
67. D. Ayodhya and G. Veerabhadram, *J. Mater.*, **5**, 446 (2019).
68. P. S. Thind, D. Kumari and S. John, *J. Environ. Chem. Eng.*, **6**, 3602 (2018).
69. D. Majhi, Y. P. Bhoi, P. K. Samal and B. G. Mishra, *Appl. Surf. Sci.*, **455**, 891 (2018).

Supporting Information

Photocatalytic degradation of the organophosphorus insecticide chlorpyrifos in aqueous suspensions using a novel activated carbon ZrO_2-ZnO nanocomposite under UV light

Soremo L Ezung, Mridushmita Baruah, Suraj Kumar, Shisak Sharma, and Dipak Sinha[†]

Department of Chemistry, Nagaland University, Lumami-798627, Nagaland, India
(*Received 4 July 2022 • Revised 15 November 2022 • Accepted 21 November 2022*)

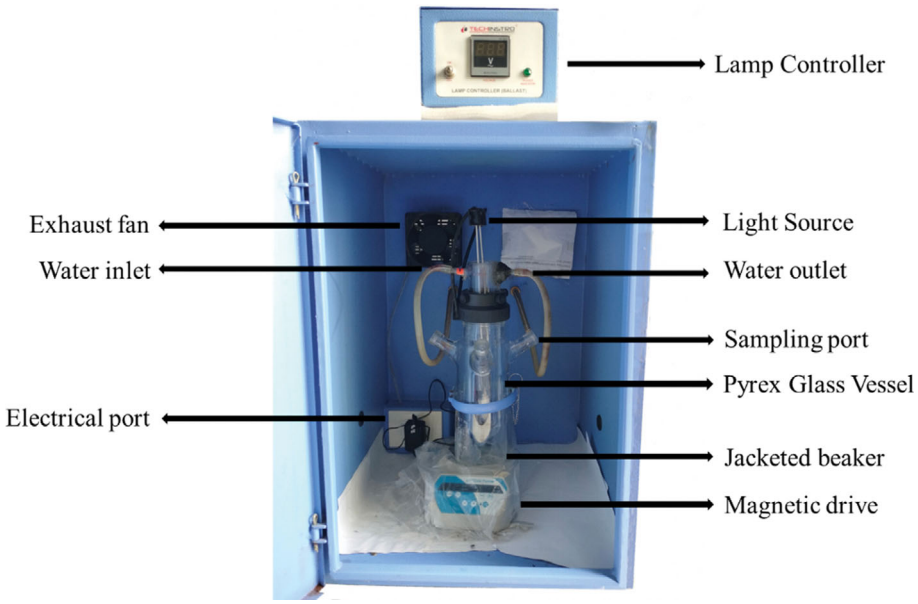

Fig. S1. Schematic experimental setup for UV light photocatalytic device.

Table S1. The properties of the ZrO_2 compound are given below

Appearance (Colour)	White
Appearance (Form)	Amorphous compound
Assay (purity)	min 99.5%
particle size	<100 nm

Table S2. LC-MS analysis of photodegraded chlorpyrifos

Sl. No.	Photodegradation products	m/z	Probable structure
1	O-(5,6-dichloro-3-hydroxypyridin-2-yl) O,O-diethyl phosphorothioate	332	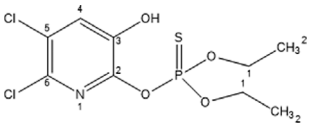
2	O-(6-chloro-3,5-dihydroxypyridin-2-yl) O,O-diethyl phosphorothioate	312	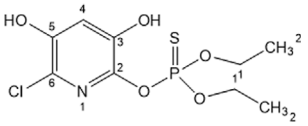
3	O-(5,6-dichloro-3-hydroxypyridin-2-yl) O,O-dihydrogen phosphorothioate	270.5	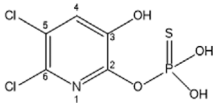
4	O,O-diethyl O-hydrogen phosphorothioate	169.3	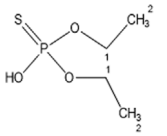
5	5,6-Dichloropyridin-3-ol	163.2	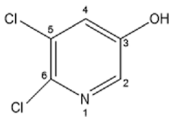
6	2-Chloropyridine-3,5-diol	144.4	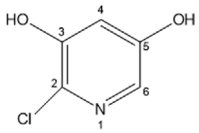
7	Pyridine-2,3,5-triol	128	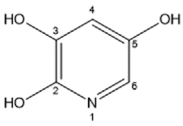
8	Phosphorothioic O,O,O-acid	114.2	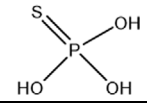
9	Phosphoric acid	97	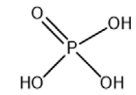
10	Pyridine	79.3	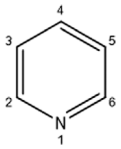
11	2-Aminoethan-1-ol	62	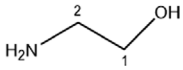
12	Acetic acid	60.3	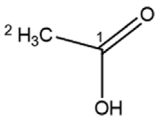
13	Ethanol	46.5	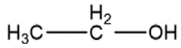

Table S3. Calculated molecular properties of ZrO_2-ZnO and SWAC/ZrO_2-ZnOnanocomposite

System	Dipole moment				Frontier orbital and energy gap		
	X	Y	Z	Total dipole moment (Debye)	HOMO (eV)	LUMO (eV)	Energy gap (eV)
ZrO_2-ZnO	−2.5874	−18.8411	0	19.0179	−0.14267	−0.08522	0.05745
SWAC/ZrO_2-ZnO	36.9314	3.1858	−3.2303	37.2082	−0.19174	−0.16810	0.02364